

Supplementary Materials for

Structure of CD20 in complex with the therapeutic monoclonal antibody rituximab

Lionel Rougé, Nancy Chiang, Micah Steffek, Christine Kugel, Tristan I. Croll, Christine Tam, Alberto Estevez, Christopher P. Arthur, Christopher M. Koth, Claudio Ciferri, Edward Kraft, Jian Payandeh*, Gerald Nakamura*, James T. Koerber*, Alexis Rohou*

*Corresponding author. Email: rohou.alexis@gene.com (A.R.); koerber.james@gene.com (J.T.K.); nakamura.gerald@gene.com (G.N.); payandeh.jian@gene.com (J.P.)

Published 20 February 2020 on *Science* First Release
DOI: 10.1126/science.aaz9356

This PDF file includes:

Materials and Methods
Tables S1 to S4
Figs. S1 to S7
References

Materials and Methods

Recombinant expression of CD20 constructs

All CD20 human constructs were synthesized (Genescript) and cloned into a modified pAcGP67A vector downstream of the polyhedron promoter. All mutations were performed using

5 Quickchange mutagenesis kit (Qiagen). Recombinant baculovirus was generated using the Baculogold system (BD Biosciences) following standard protocols. *Trichoplusia ni* cells were infected for protein production and harvested 48 hrs post-infection.

Sequence of the construct for structural studies is (the underlined sequence is the 6-His affinity tag and TEV protease cleavage site):

10 MGSTQSFFMRESKTLGAVQIMNGLFHIALGGLLMIPAGIYAPICVTWYPLWGGIMYIISGSLLAATEKNSRK
CLVKGKMMNSLFAAISGMILSIMDILNIKISHFLKMESLNFIRAHTPYINIYNCEPANPSEKNSPSTQYCYSI
QSLFLGILSVMLIFAFFQELVIAGIVENEWKRTCSRPKSNIVLLSAEEKKEQTIEIKEEVVGLTETSSQPKNEEDIEI
IPIQEEEEEEETTNFPEPPQDQESSPIENDSSPGNSENLYFQGHHHHHHHHH

15 Sequence of the construct for binding studies is (the underlined sequence is the Flag affinity tag while the Avitag is in bold):

MDYKDDDKGENLYFQS**GLNDIFEAQKIEWHEGSMTPRNSVNGTFPAEPMKPIAMQSGPKPLFRRMS**
SLVGPTQSFFMRESKTLGAVQIMNGLFHIALGGLLMIPAGIYAPICVTWYPLWGGIMYIISGSLLAATEKNSR
KCLVKGKMMNSLFAAISGMILSIMDILNIKISHFLKMESLNFIRAHTPYINIYNCEPANPSEKNSPSTQYCYSI
QSLFLGILSVMLIFAFFQELVIAGIVENEWKRTCSRPKSNIVLLSAEEKKEQTIEIKEEVVGLTETSSQPKNEEDIEI

20 IPIQEEEEEEETTNFPEPPQDQESSPIENDSSPGNS

Purification of CD20 for structural studies

Trichoplusia ni cells expressing CD20 were resuspended in 25 mM Tris pH 7.5, 150 mM NaCl (Buffer A) supplemented with cOmplete EDTA-free protease-inhibitor cocktail tablets (Roche).

25 Cell suspension was passed through a microfluidizer once at a pressure setting of 15,000 psi. Following cell lysis, suspension was spun down at 8,000 rpm for 20 min. Supernatant was then spun down 40,000 rpm at 4 °C for 1 hour. Isolated membranes were resuspended into Buffer A supplemented with 1% (w/v) GDN (Anatrace) and 0.2% (w/v) cholesterol hemisuccinate and solubilization was carried out with gentle agitation for 2 hrs at 4 °C. After ultracentrifugation at

30 40,000 rpm at 4 °C for 30 min, clarified supernatant was mixed gently with Ni-NTA resin (Sigma) pre-equilibrated with Buffer B (25 mM Tris pH 7.5, 150 mM NaCl, 0.02% GDN) for 1 hour at 4 °C. Ni-NTA resin was collected by gravity flow and washed with 5 column volumes of Buffer B supplemented with 45 mM imidazole. His-tagged CD20 was eluted with Buffer C (25 mM Tris pH 7.5, 150 mM NaCl, 0.02% GDN and 250 mM imidazole). Eluate was passed over a Superdex

35 S200 10/300 GL column (GE Healthcare) equilibrated in Buffer B and peak fractions were collected and incubated overnight with His-tag TEV protease (prepared in-house). Cleaved mixture was then passed over a fresh Ni-NTA column equilibrated with Buffer B and column was washed and eluted as described above. Flow through and wash fractions (containing untagged CD20) were collected, concentrated using an Amicon Ultra-15 Centrifugal Filter Units

40 (100K MWCO, Millipore Sigma) and loaded onto a Superose 6 10/300 GL column (GE Healthcare) pre-equilibrated with Buffer B.

Purification of CD20 for binding studies

Trichoplusia ni cells were co-infected with virus expressing full length CD20 (containing a C-terminal Flag followed by an Avi-tag) along with a virus encoding for the protein BirA. Cells were resuspended in 25 mM Tris pH 7.5, 150 mM NaCl (Buffer A) supplemented with cOmplete EDTA-free protease-inhibitor cocktail tablets (Roche). Cell suspension was passed through a microfluidizer once at a pressure setting of 15,000 psi. Following cell lysis, suspension was spun down at 8,000 rpm for 20 min. Supernatant was then spun down 40,000 rpm at 4° for 1 hour. Isolated membranes were resuspended into Buffer A supplemented with 1% (w/v) GDN (Anatrace) and 0.2% (w/v) cholesterol hemisuccinate and solubilization was carried out with gentle agitation for 2 hrs at 4°C. After ultracentrifugation at 40,000 rpm at 4°C for 30 min, clarified supernatant was mixed gently with anti-M2 FLAG resin (Sigma) pre-equilibrated with Buffer B (25 mM Tris pH 7.5, 150 mM NaCl, 0.02% GDN) for 1 hr at 4°C. Flag resin was collected by gravity flow and washed with 5 column volumes of Buffer B. Flag-tagged CD20 was eluted with Buffer C (25 mM Tris pH 7.5, 150 mM NaCl, 0.02% GDN and 0.15 mg/mL Flag peptide). Eluate was passed over a Superose 10/300 GL column (GE Healthcare) equilibrated in Buffer B and peak fractions were collected.

Expression and purification of recombinant antibodies and fragments

Constructs suitable for periplasmic expression of Fab in *Escherichia coli* and containing sequences coding for either Fab fragments of RTX or OBZ were cloned; they were transformed into 34B8 *E. coli* cells and expressed at 30°C under control of the phoA promoter in CRAP phosphate-limiting autoinduction medium (29) supplemented with carbenicillin (50 µg/mL). After 24 hr, cells were harvested and resuspended in PBS supplemented with one complete EDTA-free Protease Inhibitor Cocktail tablet (Roche) per 50 mL of lysis buffer, lysozyme (0.1 mg/mL), and benzonase (0.01 mg/mL). The prepared suspension was microfluidized at 15,000 psi and clarified at 50,000 x g for 30 min at 4°C. The supernatant was then resolved on protein G Sepharose beads equilibrated with PBS, using 2 mL packed resin volume per original gram of cell paste. The column was washed extensively with PBS and Fabs were eluted under mildly acidic conditions (0.56 % glacial acetic acid pH 3.6). Eluted Fabs were immediately dialyzed overnight at 4°C against buffer containing 500 mM NaCl, 10% glycerol, and 100 mM Tris (pH 8.0). Fabs was further resolved on an S75 16/60 gel filtration column (GE Healthcare) using PBS (pH 7.2) as the running buffer.

Constructs for mammalian expression of IgGs were generated by gene synthesis. Plasmids encoding for the LC and HC were co-transfected into 293 cells and purified with affinity chromatography followed by SEC using standard methods (MabSelect SuRe; GE Healthcare, Piscataway, NJ, USA).

CDC assay

A complement dependent cytotoxicity (CDC) assay was set up to measure the degree of antibody dependent complement lysis of target cells. Human serum complement protein C1q, that binds to the Fc domain of an antibody bound to a target cell, was used to trigger the initiation of the complement cascade. This action eventually culminates in the formation of the complement protein membrane attack complex resulting in target cell lysis. The assay is

performed in a 96 microwell plate format and in duplicate/triplicate as follows. 50 µL of serially diluted (1:3) anti-CD20 mAbs and controls starting at 900 nM were incubated with 50 µL of B-cell lymphoma WILS-2 (ATCC CRL-8885) cells (50,000) and with 50 µL of a 1:2 dilution of normal human serum complement (Quidel, Santa Clara, CA). After a 2-hour incubation at 37°C, 15 µL

5 of Alamar Blue (Biosource International, Camarillo, CA) was added and incubated for an additional 18 hours at 37 C. The plates were briefly shaken for 15 minutes and then read on a fluorescent plate reader (Ext. 535 nm, Emt 590 nm) to determine the relative fluorescent units (RFU). The RFU value observed was plotted relative to concentration of mAb in KaleidaGraph (Synergy Software, Reading, PA). Curves are plotted using a 4-parameter fit.

10

Flow cytometry assay

The relative degree of anti-CD20 mAbs binding to CD20 expressing B-cell lymphoma cell lines was measured by flow cytometry. Antibodies were serially diluted 1:2 in phosphate buffered saline containing 1% of heat inactivated fetal bovine serum (VWR Int. Radnor, PA). 50 µL of the 15 diluted mAbs was dispensed into U-bottom 96-well plates. The concentrations ranged from 200 nM to 0.82 nM. Next, each well received 100,000 WIL2-S (ATCC CRL-8885) B-cell lymphoma cells in a 50 ul volume. The plates were gently mixed and incubated on ice. Following a 1-hr 20 incubation, the cells were pelleted and washed 5 times in cold PBS. 1 ug of a FITC-conjugated goat anti-human Fc specific F(ab')² (Jackson Immunoresearch, West Grove, PA) was added to each well. After a 30-minute incubation on ice, the cells were pelleted, washed in cold PBS 3-times and then fixed in PBS containing 4% paraformaldehyde (ThermoScientific, Rockford, IL). Cells were analyzed using a BD Biosciences LSRII Fortessa (San Jose, CA) to determine the geometric MFI (median, fluorescence intensity) of antibody binding to cells.

25

BLI binding studies

Biotinylated CD20 was captured on streptavidin SA biosensors (FortéBio / Molecular Devices) at 10 µg/mL for 180 seconds and washed to remove any unbound material before conducting measurements in Buffer B supplemented with 0.5 mg/mL BSA. The kinetic data were fit to a simple 1:1 binding model to determine the affinity constant (K_D) using the association (K_{on}) and 30 dissociation (K_{off}) rates. Binding assays were performed in triplicate and average KD values reported with SDs. Buffer containing 0.02% GDN supplemented with 0.002% CHS was used for all washes and dilutions. Sensorgrams were normalized to a reference well containing only buffer.

35

SPR binding studies

Binding studies were conducted using on a 8K Biacore instrument by immobilizing onto a Sensor Chip C1 (GE LifeSciences), which had been immobilized with 500-800 RU of neutravidin. The N-terminal avi-tagged CD20 was immobilized in the presence of 50 mM HEPES pH 7.5, 150 mM NaCl, 0.2% GDN to a density ~40 RU. A amino-terminally biotinylated (PEGx6) linear 40 peptide with the CD20 epitope (¹⁶³NIYNCEPANPSEKNSPSTQYCYSIQ¹⁸⁷), which had been synthesized using standard solid-phase Fmoc chemistry and purified with reverse phase HPLC (30), was immobilized under similar conditions to a density of ~15 RU. The full length IgG and Fab fragments were added using single cycle kinetic methods with 100 second associations at

20 °C and 500 s dissociation phase at 50 µL/min depending. The data was referenced to an un-immobilized neutravidin surface and a blank injection. Non-specific binding to the chip surface was subtracted from each curve. Data was analyzed using Biacore Evaluation software and curves were fit using 1:1 and 2-state kinetic fits.

5

Complex formation

Recombinant CD20 was incubated with a molar excess of IgG or Fab and incubated on ice for 30 min. Reaction was passed over a Superose 6 10/300 GL column (GE Healthcare) equilibrated in 25 mM Tris pH 7.5, 150 mM NaCl, 0.02% GDN and peak fractions were collected.

10

Negative stain analysis

Complexes were diluted to 0.01 mg/mL in buffer B and 4 µL of the solution was placed onto a CF2/1 300 grid from Electron Microscopy Sciences (EMS) previously cleaned using a GloQube glow discharge (Quorum Technologies) system. After 30 sec incubation, sample was blotted with Whatman paper, dipped three times into 30 µL of distilled water and stained twice into 30 µL of a filtered solution of 2% uranyl acetate. Grids were imaged using a 200 KV Talos F200c with a CETA camera (ThermoFischer Scientific) and 2D class averages were computed using cistem (31).

20

Differential scanning fluorimetry

Melting experiments were conducted on a Prometheus NT48 (NanoTemper technologies) by measuring the tryptophan fluorescence 330/350 nm ratio of protein samples concentrated at 0.3 mg/mL in a standard capillary.

25

SEC-MALS analysis

Purified proteins and complexes were run on a Waters XBridge BEH S200 A gel filtration column equilibrated in 25 mM Tris pH 7.5, 150 mM NaCl, 0.02% GDN in line with a Dawn HELEOS II (Wyatt Technologies) light scattering detector connected to a Wyatt OptiLab rEX refractive index detector. Wyatt Technologies software (ASTRA) was used to determine the corresponding peaks' molecular weight based on the refractive index. In order to determine the unbiased molecular weight of the apo CD20 protein, the protein conjugate analysis within the ASTRA software was performed. Because the dn/dc value for this detergent is unknown, a value of 0.143 mL/gm was arbitrary used to calculate the molecular weight of the GDN micelle (dn/dc values for most detergents is usually comprised between 0.1 and 0.15 ml/gm).

35

Cryo-EM sample preparation and data acquisition

Recombinant CD20 was incubated with Rituxan Fab at 1:1.2 molar ratio and incubated on ice for 30 min. Mixture was injected over a Superose 6 Increase 3.2/300 column (GE Healthcare) equilibrated in 25 mM Tris pH 7.5, 150 mM NaCl, 0.01% GDN. 3.5 µL of the peak fraction of CD20/Rituxan Fab complex at a concentration of 2 mg/mL was applied to a glow-discharged C-flat holey carbon grid (CF-1.2/1.3-2C, Electron Microscopy Sciences) coated with a thin layer of gold. Grids were blotted in Vitrobot Mark IV (ThermoFisher Scientific) using 5 s blotting time with 100% humidity, and then plunge-frozen in liquid ethane cooled by liquid nitrogen. A total

of 24,743 movie stacks were collected with SerialEM (32) on a Titan Krios (Thermo Fisher Scientific) operated at 300 kV and equipped with a BioQuantum energy filter operated with a 20eV energy slit with a K2 Summit direct electron detector camera (Gatan). Images were recorded at a nominal magnification of 165000 x, corresponding to a pixel size of 0.849 per 5 pixel. Each image stack contains 40 frames recorded every 0.25 s giving an accumulated dose of 53 electrons/Å² and a total exposure time of 10 s. Images were recorded with a set defocus range of 0.5 to 1.5 μm.

Structure determination

10 All image processing was performed with cisTEM (31). For the 3D structure of CD20 bound by RTX Fab, the processing scheme was as depicted in Figure S3C. For atomic model building, PDB 2OSL was used to place the ECL2 peptide epitope and an initial model of CD20 was built by extending this manually in Coot (33). The model for the RTX Fab was started from PDB 4KAQ. This complete model was then rebuilt using interactive molecular dynamics (34), and refined in 15 real space (35).

Structure analysis

Protein-protein shape complementarity was calculated using the program SC (36). Figure preparation and computation of buried solvent-accessible surface area was done with 20 ChimeraX (37). 3D homology structural alignments were performed using the DALI server (38) and sequence alignments was using EMBL-EBI's Clustal Omega Multiple Sequence Alignment tool (39) followed by structure-guided manual curation.

Table S1: MALS estimates of CD20:Fab molecular weights

	Estimated molecular weight of complex (kDa)	Relative to apo CD20 (kDa)
CD20	308.7 (\pm 3.7 %)	0.0
CD20 + RTX Fab	386.7 (\pm 3.8 %)	78.0
CD20 + OBZ Fab	348.2 (\pm 3.6 %)	39.5

Estimated MW includes CD20's detergent GDN micelle and does not correspond to the protein molecular weight.

5 Table S2: Affinity of mAbs to immobilized full-length CD20

mAb	K _D (nM)	Average SE (%)	Kinetics Chi ² (RU ²)
RTX	1.65	3.44	0.36
OBZ	12.33	1.01	0.10
RTX (Fab)	21.4	0.55	0.22
OBZ (Fab)	58.8	0.55	0.47
RTX HC.Y97F	24.75	3.77	1.21
RTX HC.Y97S	> 1500	N/A	N/A
RTX HC.S31E	100.35	1.82	1.01
RTX HC.G99K	468.5	0.59	0.24
RTX LC.S28D	37.95	2.93	1.21
RTX LC.S31D	136	2.79	1.17

Surface plasmon resonance measurements of mAb affinity for CD20. For each parameter, the average value (n=2) is shown. Data were fit using a two-state reaction model for all molecules tested. A 1:1 binding model did not fit well to either RTX or OBZ sensorgrams (data not shown).

10

Table S3: Affinity of mAbs to immobilized CD20 epitope peptide

mAb	K _D (μ M)	Average SE (%)	Kinetics Chi ² (RU ²)
RTX	0.642	18	0.797
OBZ	0.347	16	4
RTX HC.Y97F	1.21	9.7	0.06
RTX HC.Y97S	No binding	N/A	N/A
RTX LC.S28D	2.31	12.8	0.013
RTX LC.S31D	3.75	15.9	0.0128

Surface plasmon resonance measurements of IgG affinity for CD20 peptide were fit using a 1:1 steady state model.

15

Table S4: cryoEM

Data collection		
5	Microscope	ThermoFisher Titan Krios
	Acceleration voltage	300 kV
	Detector	Gatan K2
	Energy filter	Gatan BioQuantum
10	Energy filter slit width	20 eV
	Image pixel size	0.849 Å
10	Electron exposure	48.5 e ⁻ /Å ²
	Number of frames	40
Image processing		
15	Number of micrographs	24,743
	Number of picks ("soft disc" template)	4,114,800
	Number of particles used	466,362
	Pixel size for processing & reconstruction	1.0 Å
	Box size	310 pixels
20	Symmetry	C2
	Number of particles for final reconstruction	155,719
	Highest resolution used in refinement	5.0 Å
	Global resolution (FSC = 0.143)	3.3 Å
Model building & refinement		
25	Software used (de novo build)	coot
	Software used (refinement)	ISOLDE, Phenix
	Number of amino acid residues	1,196
Model validation (Molprobity)		
30	MolProbity score	1.54
	All-atom clashscore	4.71
	Ramachandran plot	
	favored	95.72 %
	allowed	4.19 %
35	outliers	0.08 %
	Rotamer outliers	0.49 %
	Cβ deviations	0.72 %
	Peptide plane	
	cis-proline	15.25 %
40	cis-general	0.00 %
	twisted proline	0.00 %
	twisted general	0.00 %
	CaBLAM outliers	1.10 %

Supplementary Figure legends

Figure S1. CD20 constructs, expression, purification and characterization. **A.** Topological map of CD20 constructs used in this study. The construct used for EM studies was amino-terminally truncated at residue Thr41, and carboxy-terminally His-tagged. The full-length construct was N-terminal FLAG-Avi-tagged for binding studies. **B.** Primary sequence of CD20, annotated with secondary-structure elements. Amino acid residues involved in interactions with RTX Fabs are labeled in pink (light chain) or purple (heavy chain). **C.** SEC-MALS analysis of detergent-solubilized, purified CD20 reveals a protein molecular mass of approximately 67 kDa, consistent with a CD20 dimer. Estimated molecular weight of CD20 embedded within a detergent micelle was determined by subtracting the estimated size of the GDN micelle using the “protein conjugate” feature of the ASTRA software (Wyatt Technology). An arbitrary dn/dc value of 0.143 mL/g was attributed to GDN. **D.** SEC elution profiles of CD20 alone (blue), CD20 with OBZ Fab (red), or CD20 with RTX Fab (black) show that RTX and OBZ Fabs form stable complexes with purified CD20, and that the CD20:RTX complex is of larger dimensions than the CD20:OBZ complex. **E.** BLI equilibrium values from Figure 1A are plotted as a function of Fab concentration, indicating that approximately 2 times more RTX than OBZ Fabs bind to immobilized CD20. Fitting of these data with a 1:1 binding model suggests apparent K_D values of 49 nM for RTX and 70 nM for OBZ. **F.** SDS-PAGE analysis of recombinant wild type full length CD20 and Tyr182Cys mutant under non-reducing and reducing conditions (10 mM TCEP, 5 minutes). Under native conditions, Tyr182Cys mutant runs at a molecular weight consistent with a CD20 dimer; upon addition of reducing agent, band collapses down to the equivalent of a CD20 monomer suggesting mutant was expressed as a disulfide linked dimer. Migration of wild type protein is unchanged regardless of the reducing conditions.

Figure S2. Cholesterol hemisuccinate stabilizes CD20. **A.** Experimental workflow of sample preparation. Full length CD20 was solubilized in 1% GDN in absence or presence of 0.2% CHS and purified over Ni-NTA column. Concentrated eluates were then diluted 100 fold into CHS free buffer (blue or orange traces, respectively) or into buffer supplemented with 0.002% CHS (red and black traces). Standard error was calculated from three technical replicates. **B.** Differential scanning fluorimetry of CD20 purified in presence or absence of cholesterol measured on NanoDSF instrument. Curves are average of three replicates. For cryoEM studies, CHS was added at the time of solubilization.

Figure S3. CryoEM structure determination of CD20:RTX Fab. **A.** Representative micrograph. **B.** Representative 2D class averages. **C.** Single-particle image processing workflow. **D.** Fourier Shell Correlation (FSC) between two half datasets yields a global resolution estimate of ~ 3.3 Å. No spatial frequencies beyond $1/5 \text{ Å}^{-1}$ were used at any point during refinement. **E.** Heat map representation of the distribution of assigned particle orientations shows a bias towards side views (near the periphery of the plot). **F.** Isosurface rendering of the 3D map with surface coloring according to the local resolution estimated by windowed FSCs (40). **G.** Map details showing side chains in stick representation and a mesh representation of

the 3D Coulomb potential map, contoured at the indicated σ level (where σ is one standard deviation above the mean of the map values).

Figure S4. The MS4A family and nearest structural homologues of CD20. **A.** Multi-sequence alignment of CD20 (MS4A1) and selected members of the MS4A family. Clustal conservation is denoted by asterisk (*; fully conserved residue), colon (:; strongly similar properties), period (.; weakly similar properties). **B.** Cartoon renderings of CD20 and the two closest structural homologues identified, claudin-3 and CD81. In the case of claudin-3, sequence or topology-based alignments do not give good structural overlap (“topological alignment”); a slightly better 3D alignment can be obtained by ignoring the sequence and connectivity of the TM helices (“3D TM alignment”).

Figure S5. The CDR surface of RTX is also involved in mediating Fab:Fab contacts in crystallography experiments. **A.** Bottom and side views of RTX Fab in complex with CD20 or ECL2 peptide, as visualized with cryoEM (this work) or X-ray crystallography (4) respectively. For clarity and ease of comparison, the non-ECL2-turret parts of CD20 are hidden from the cryoEM structure. The structures were aligned by superposing CD20 residues 170 to 175, which constitute the core of the main RTX epitope. **B.** Heavy-chain loop 3 adopts significantly different conformations in the cryoEM and X-ray crystallography structures.

Figure S6. Sequence analysis of RTX and other anti-CD20 antibodies. **A.** Sequences of RTX and mouse germline. **B.** Multi-sequence alignment of notable anti-CD20 antibodies. Type I antibodies with overlapping ECL2 turret epitopes are shown in black. Ofatumumab, which is also a type I antibody, but binds a composite ECL1/ECL2 epitope is shown in blue. Type II mAbs are shown in purple.

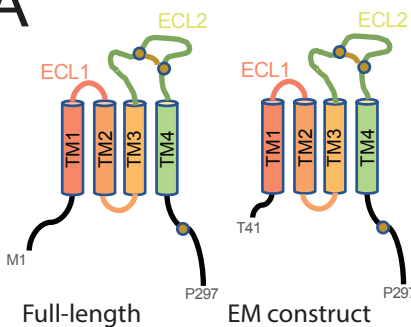
Figure S7. Full-length IgG RTX and OBZ complex formation with CD20. **A.** Size exclusion chromatography profiles of CD20 complexed with an excess of OBZ IgG (blue trace) or RTX IgG (red). CD20:RTX elution profile suggests the presence of multiple distinct species whereas CD20:OBZ co-elution peak suggests a unique species, although slightly asymmetrical. **B.** SDS-PAGE associated to SEC profiles shown in panel A. Fractions underlined corresponds to co-elution fractions. **C.** SPR sensorgram. RTX and OBZ (red and blue respectively) were injected in increasing concentrations over surface immobilized CD20. Under saturating conditions the RTX shows a 2:1 stoichiometry compared to the OBZ binding to CD20. Injection spikes were removed for clarity. **D.** Biolayer interferometry (BLI) traces representing binding of a dilution series of Rituxan IgG to immobilized biotinylated CD20. Sensograms were normalized to a reference well containing only buffer. **E.** Biolayer interferometry (BLI) traces representing binding of a dilution series of Gazyva IgG to immobilized biotinylated CD20. Sensograms were normalized to a reference well containing only buffer. **F.** BLI equilibrium values from panels D and E are plotted as a function of IgG concentration. Fitting of these data with a 1:1 binding model suggests

5

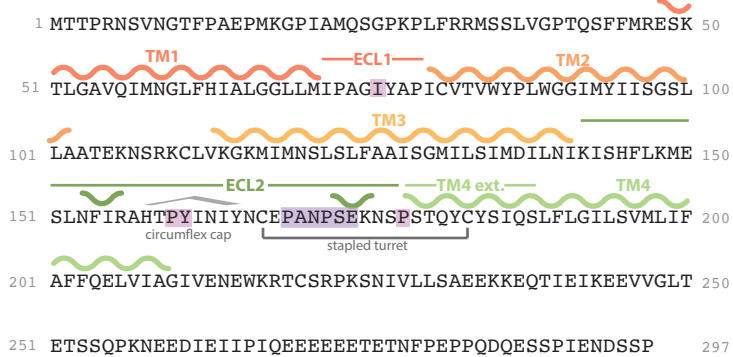
apparent KD values of 1.7 nM for RTX (red trace) and 3.3 nM for OBZ (blue traces) consistent with SPR measurements of the same (Table S2). **G.** Representative micrograph of negative-stain EM analysis of purified CD20 in complex with RTX (left) or OBZ (right) IgG (see Figure S1, panel A and B). A representative cyclical superstructure is highlighted by a white box.

Figure S1

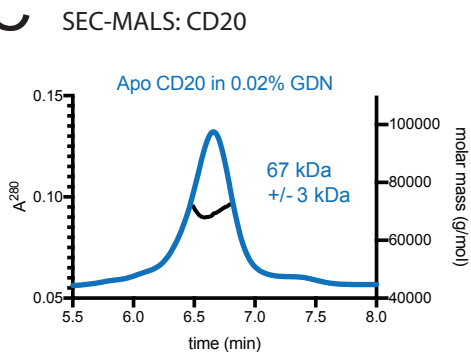
A



B

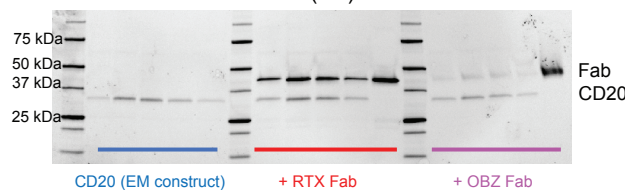
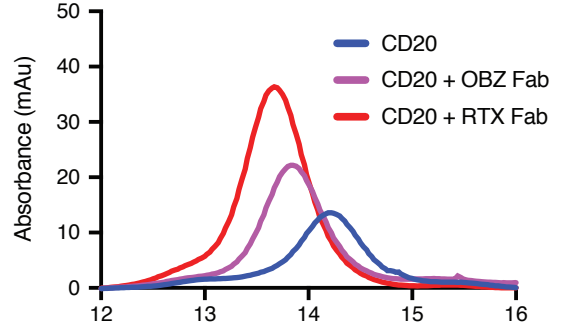


C

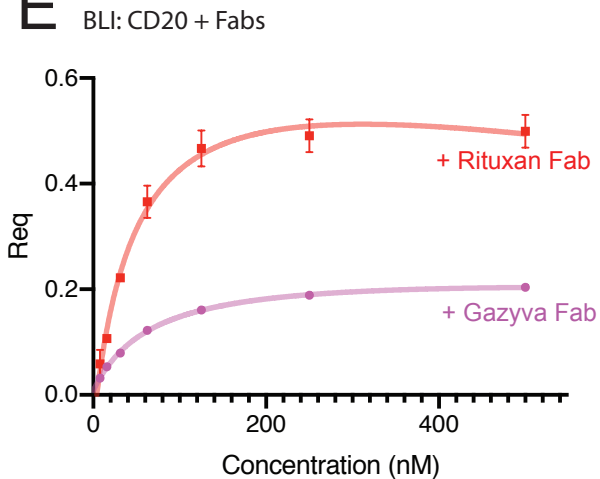


D

SEC: CD20 + Fabs (Superose 6 10/300)



E



F

SDS-PAGE: dimer mutant cross-linking

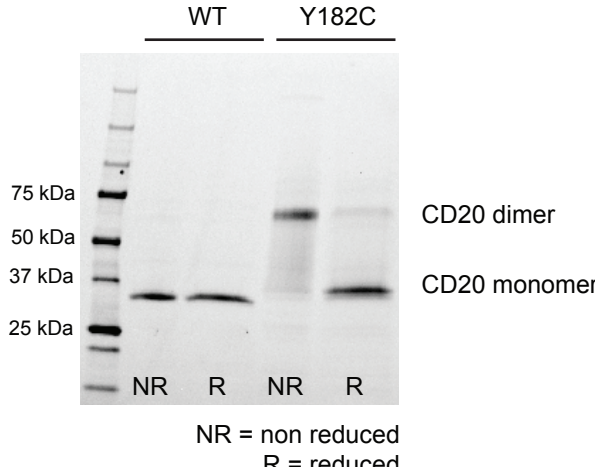
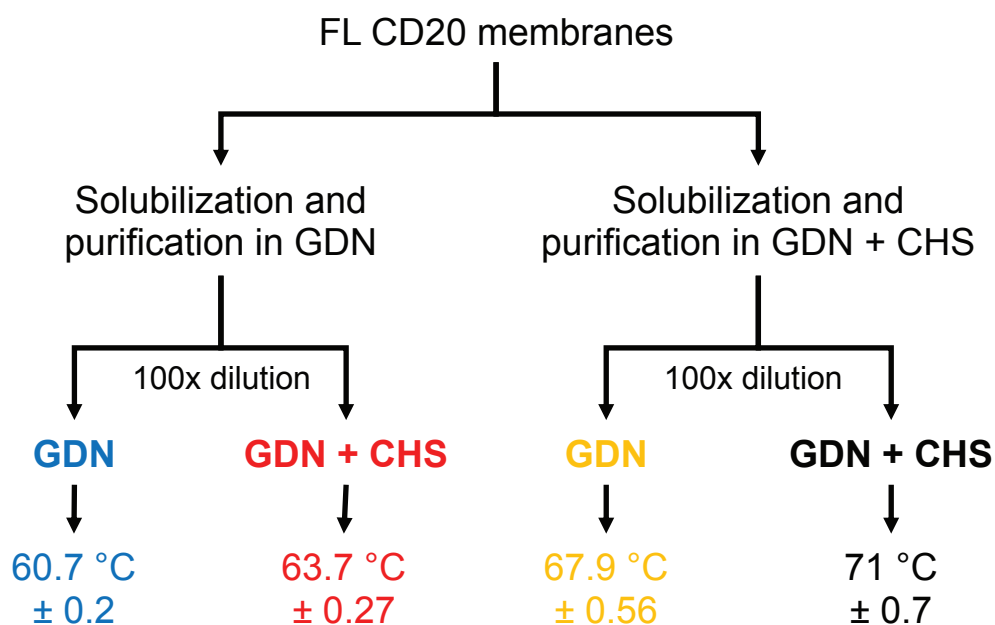


Figure S2

A



B

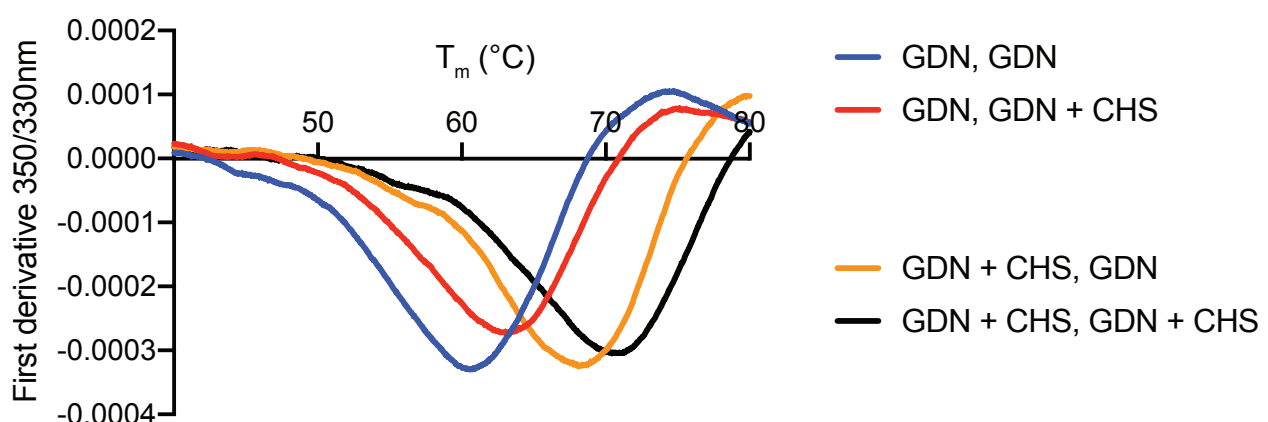
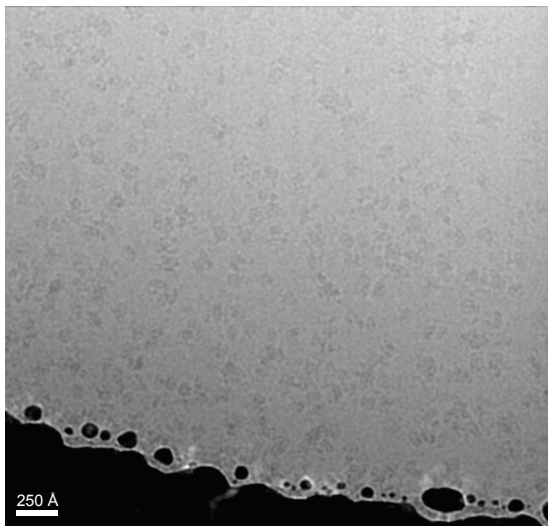
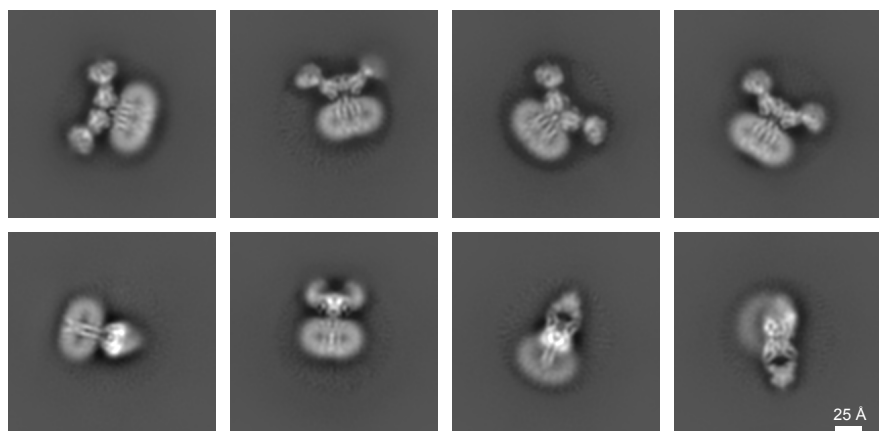


Figure S3

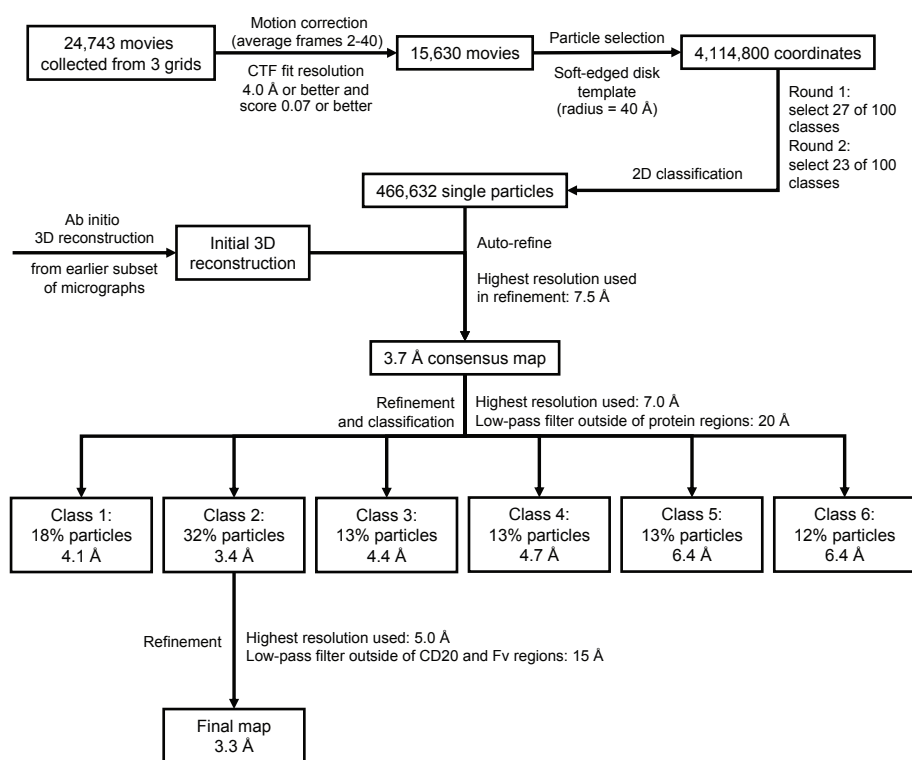
A



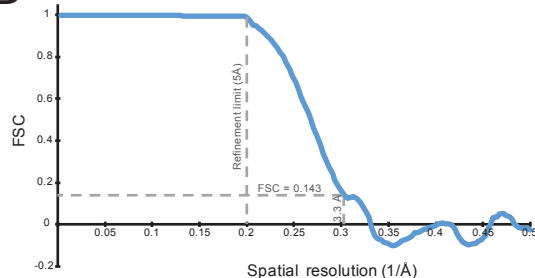
B



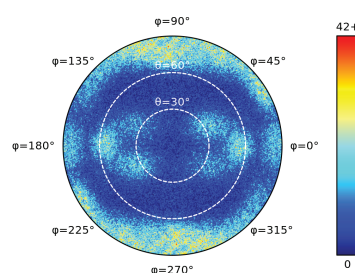
C



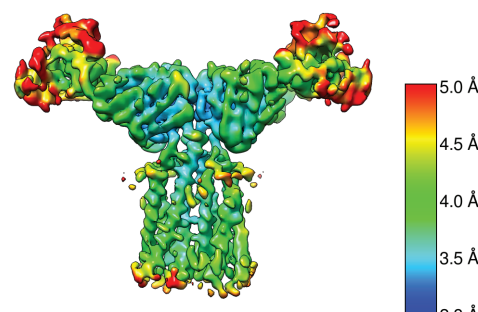
D



E



F



G

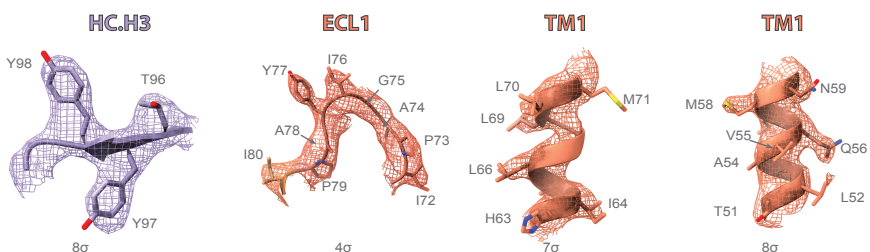


Figure S4

A

		TM1	ECL1	TM2	ECL2	TM3	TM4 ext.	TM4		
MS4A1	46	MREISITLGAQVQI	NGLFH	ALGGL	MI PAGI	YAPICVTVWYP	WGGIMYII	SGSL	LAATEKN-SRKCLVKGKMINNSL 124	
MS4A3	45	KAKLQLVLGA	IQIL	NAAMI	ALGVF	LSLQYPYHFQKHFFFFFTYGYP	IWGAVFFC	SSGTL	SVVAGIK-PTRTWLQNSFGMNIASA 129	
MS4A4A	60	KGEPKVLGVQIL	TALMS	SMGIT	MCMASN	TYGSNPISVYIGYT	IWG SVMFI	ISGS	SIAAGIR-TTKGLVRGSLGMNITSS 141	
MS4A5	44	ARKMKILGT	IQIL	FGIMT	ESFGV	FLFTLLK	PYPRFPFIFL	SGYFWGGSVL	FINSGAELIAVKRK-TTETLILS 125	
MS4A15	68	TGEPKVLGTVQIL	IGLIHL	GFGSV	LLMVRRGHVG	IFFIEGGVP	FWGGAC	FIISGS	SVAEKN-HTSCLVRSSLGTNIILS 147	
MS4A8	66	LKEGKTLGA	IQII	IGLAH	GLGSIM	ATVLVGE	YLSISFYGGFP	FWGGLWF	IIISGS	SVAAEQNQPYSYCLSGSLGLNIVSA 146
MS4A12	85	KEEAKALGVQIM	VGLMH	FGFIV	CLISFS	FREVLGF	ASTAVIGGYPFW	WGLSF	IIISGS	VSASKE-LSRCLVKGSLGMNIVSS 169
Conservation	:	:	**..::**:	.	..::*	.	..::**.	..::**:	.	.
Consensus			KGEPKVLGXIQILIGLMH	LGFGXXLLXLXG	---	XXFFXF	SFYGGPF	WGGLVXF	IIISGS	LSVAAXX-TTRCLVRGSLGMNIXSA

		TM3	ECL2	TM4 ext.	TM4								
MS4A1	125	FATISGMIISIMD	LNKISHFLKMESLN	FIRAHTPYIN	YNCCEPANPSEKN	SPSTQYCYSI	QSLFLGILSV	LIAFAFFOELVIAG 210					
MS4A3	130	TIBLVGTAFLSLN	IAVNIQ	-----	SLR	-----	SC	-----	HSSSEPDLCNYMGSI	SNGMVSL	LILTLLFCVTIS 190		
MS4A4A	142	VLAASCILINTFS	LAFY	-----	SFHHPYCNYYGNS	-----	NNCHGTM	SILMGLDGML	LLL	SVL	FCIAVS 201		
MS4A5	126	LGAIACI	ILLTFG	ILDQ	-----	NYICGY	-----	SHQNSQCKAVT	VLF	LGILIT	MTFSI	ELFISLP 183	
MS4A15	148	MAAFACTA	LLMD	FGVT	-----	N-RD	-----	VDRGYLA	V	TIETV	LB	FFTAVI 189	
MS4A8	147	ICSAVGV	ILFITD	SIP	-----	H-PYAYPDYYYA	-----	W	-----	GVNPGMAISGV	LLV	FCCL	FFGIACA 201
MS4A12	170	IL	FIGV	ILLVD	CIN	-----	G-VAG	-----	W	-----	AVLSKGKISAT	MIFSL	LLFFVACA 219
Conservation	:	*	:	..:					.	:	..::		
Consensus			ILAXXGXILLXFDXAXN	-----	X-----X	-----	-----	-----	W-X	-----	XVSIGMGIXXXLLIFS	LLEFFIAAXX	

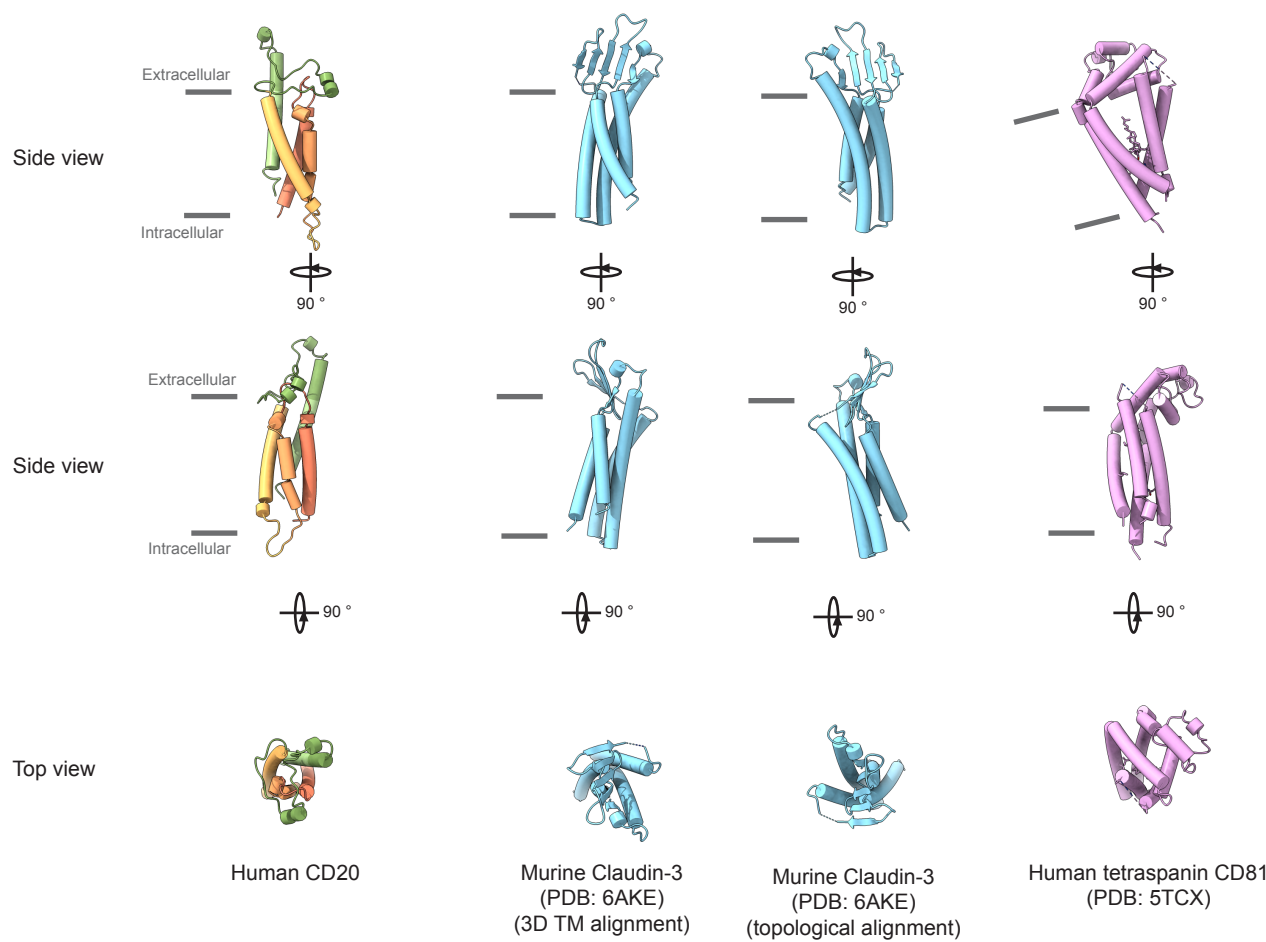
B


Figure S5

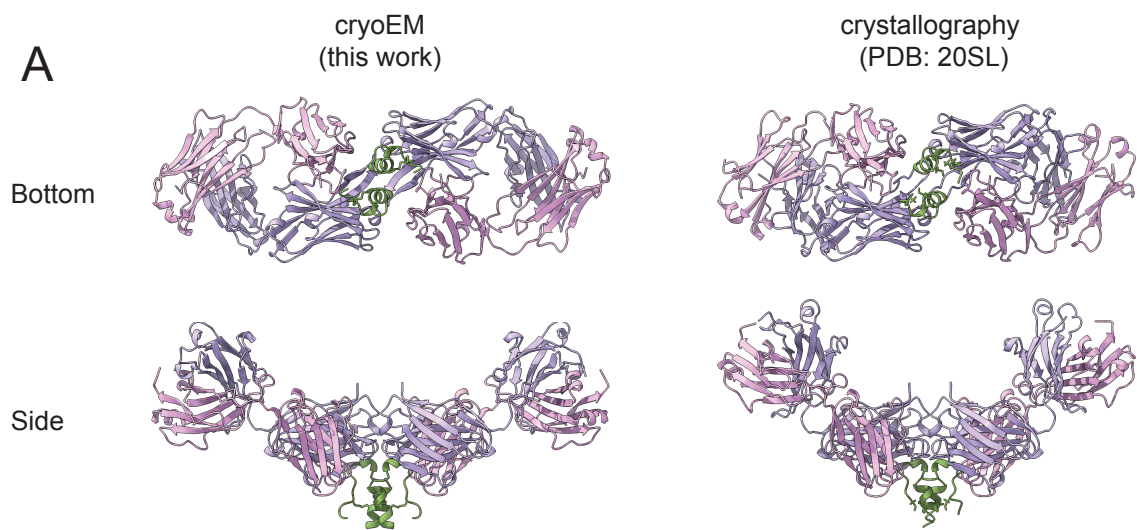
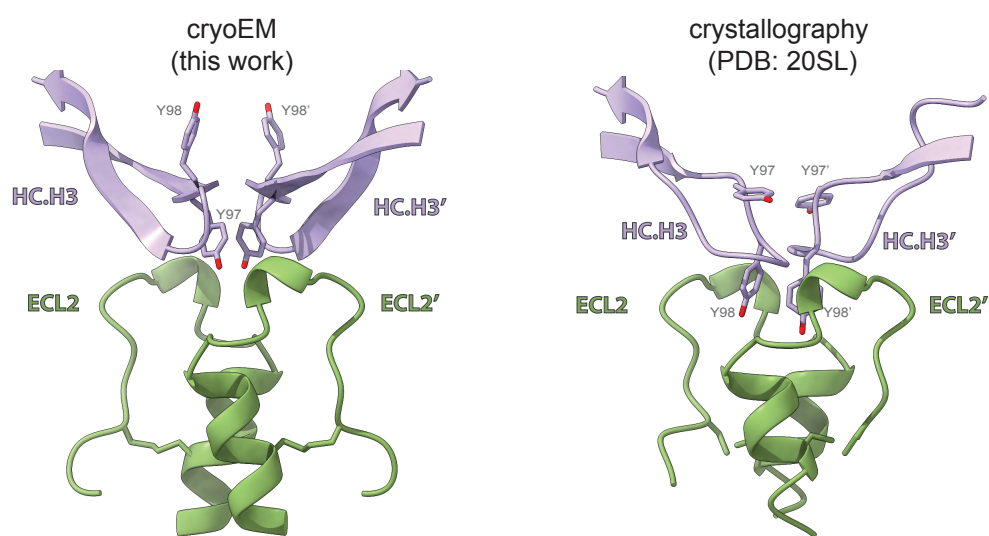
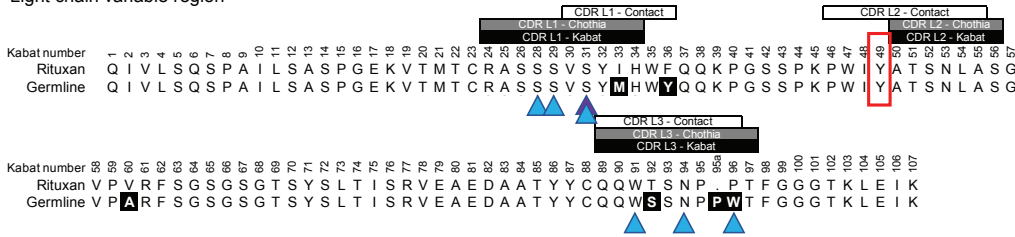
A**B**

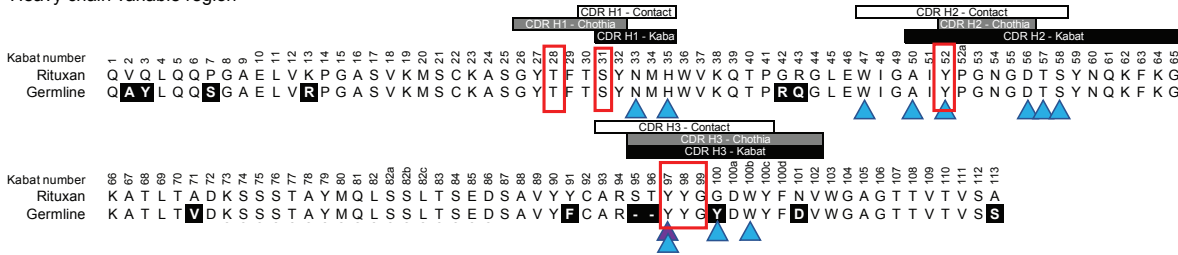
Figure S6

A

Light chain variable region

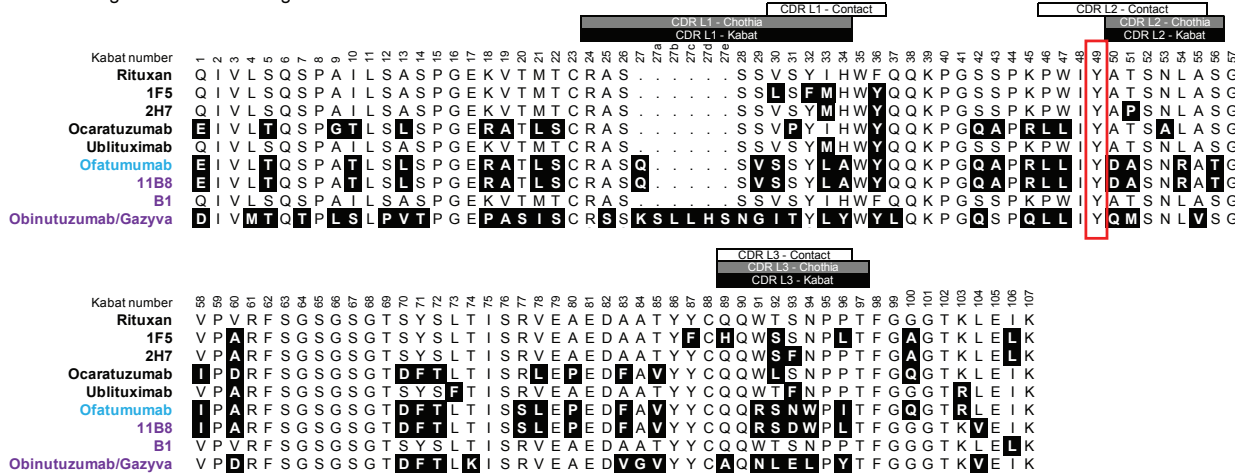


Heavy chain variable region

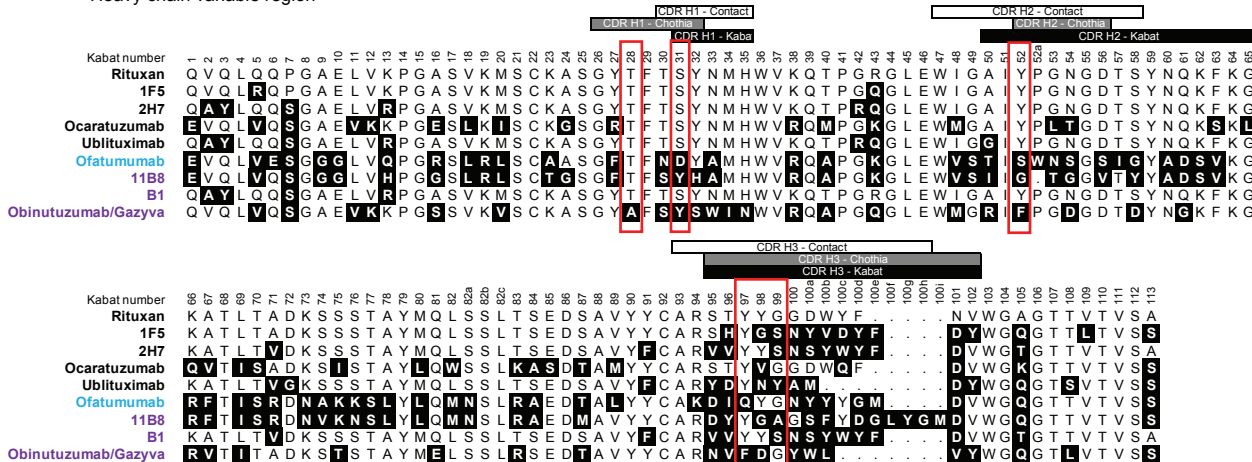


B

Light chain variable region

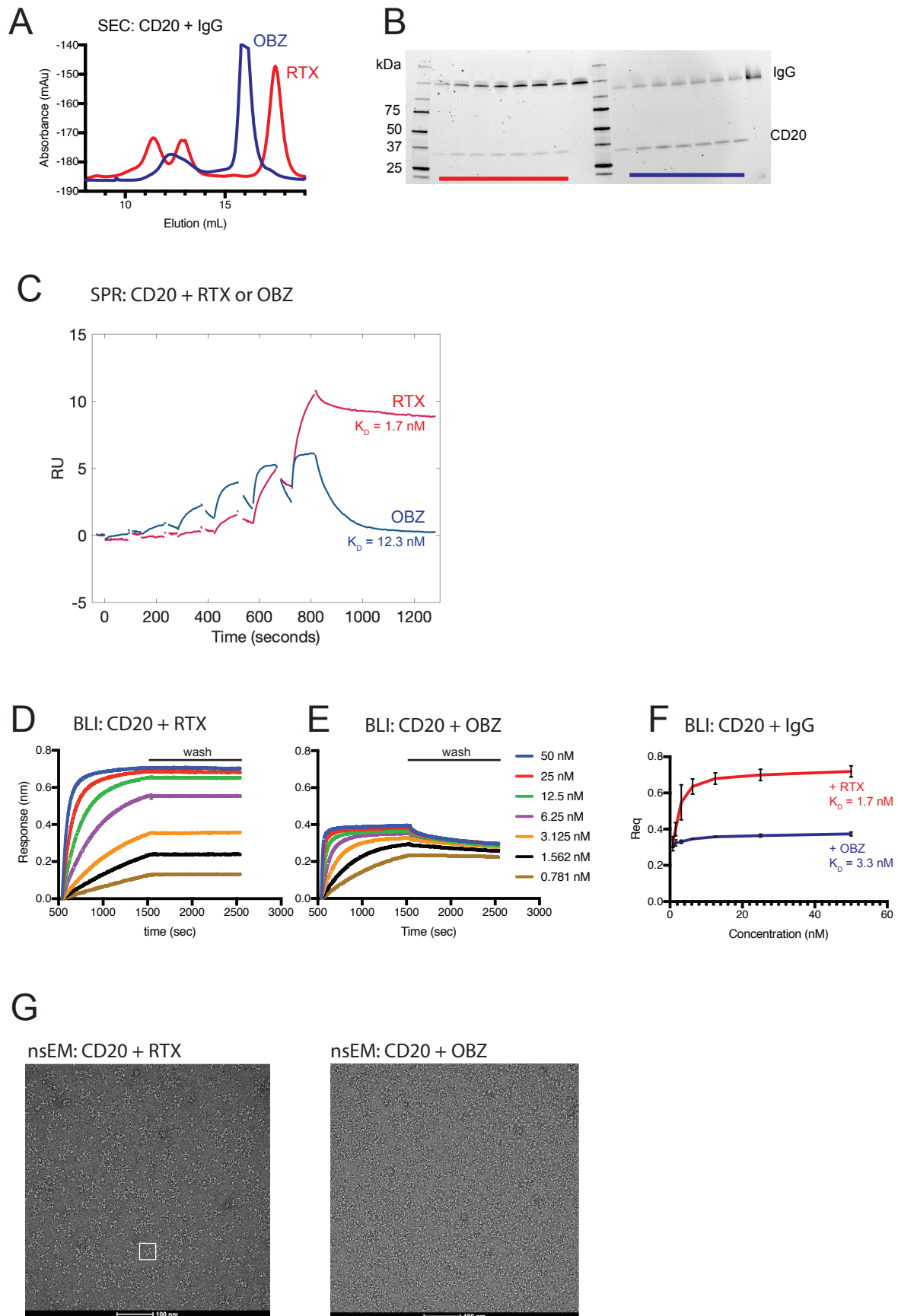


Heavy chain variable region



- ▲ Fab-CD20 interactions
- ▲ Fab-CD20' interaction
- Fab-Fab interactions

Figure S7



References and Notes

1. M. J. E. Marshall, R. J. Stopforth, M. S. Cragg, Therapeutic antibodies: What have we learnt from targeting CD20 and where are we going? *Front. Immunol.* **8**, 1245 (2017). [doi:10.3389/fimmu.2017.01245](https://doi.org/10.3389/fimmu.2017.01245) [Medline](#)
2. P. Stashenko, L. M. Nadler, R. Hardy, S. F. Schlossman, Characterization of a human B lymphocyte-specific antigen. *J. Immunol.* **125**, 1678–1685 (1980). [Medline](#)
3. L. Eon Kuek, M. Leffler, G. A. Mackay, M. D. Hulett, The MS4A family: Counting past 1, 2 and 3. *Immunol. Cell Biol.* **94**, 11–23 (2016). [doi:10.1038/icb.2015.48](https://doi.org/10.1038/icb.2015.48) [Medline](#)
4. J. Du, H. Wang, C. Zhong, B. Peng, M. Zhang, B. Li, S. Huo, Y. Guo, J. Ding, Structural basis for recognition of CD20 by therapeutic antibody rituximab. *J. Biol. Chem.* **282**, 15073–15080 (2007). [doi:10.1074/jbc.M701654200](https://doi.org/10.1074/jbc.M701654200) [Medline](#)
5. G. Niederfellner, A. Lammens, O. Mundigl, G. J. Georges, W. Schaefer, M. Schwaiger, A. Franke, K. Wiechmann, S. Jenewein, J. W. Slootstra, P. Timmerman, A. Brännström, F. Lindstrom, E. Mössner, P. Umana, K.-P. Hopfner, C. Klein, Epitope characterization and crystal structure of GA101 provide insights into the molecular basis for type I/II distinction of CD20 antibodies. *Blood* **118**, 358–367 (2011). [doi:10.1182/blood-2010-09-305847](https://doi.org/10.1182/blood-2010-09-305847) [Medline](#)
6. J. K. Bubien, L. J. Zhou, P. D. Bell, R. A. Frizzell, T. F. Tedder, Transfection of the CD20 cell surface molecule into ectopic cell types generates a Ca^{2+} conductance found constitutively in B lymphocytes. *J. Cell Biol.* **121**, 1121–1132 (1993). [doi:10.1083/jcb.121.5.1121](https://doi.org/10.1083/jcb.121.5.1121) [Medline](#)
7. M. J. Polyak, J. P. Deans, Alanine-170 and proline-172 are critical determinants for extracellular CD20 epitopes; heterogeneity in the fine specificity of CD20 monoclonal antibodies is defined by additional requirements imposed by both amino acid sequence and quaternary structure. *Blood* **99**, 3256–3262 (2002). [doi:10.1182/blood.V99.9.3256](https://doi.org/10.1182/blood.V99.9.3256) [Medline](#)
8. M. J. Polyak, H. Li, N. Shariat, J. P. Deans, CD20 homo-oligomers physically associate with the B cell antigen receptor. Dissociation upon receptor engagement and recruitment of phosphoproteins and calmodulin-binding proteins. *J. Biol. Chem.* **283**, 18545–18552 (2008). [doi:10.1074/jbc.M800784200](https://doi.org/10.1074/jbc.M800784200) [Medline](#)
9. T. W. Kuijpers, R. J. Bende, P. A. Baars, A. Grummels, I. A. M. Derkx, K. M. Dolman, T. Beaumont, T. F. Tedder, C. J. M. van Noesel, E. Eldering, R. A. W. van Lier, CD20 deficiency in humans results in impaired T cell-independent antibody responses. *J. Clin. Invest.* **120**, 214–222 (2010). [doi:10.1172/JCI40231](https://doi.org/10.1172/JCI40231) [Medline](#)
10. C. A. Walshe, S. A. Beers, R. R. French, C. H. T. Chan, P. W. Johnson, G. K. Packham, M. J. Glennie, M. S. Cragg, Induction of cytosolic calcium flux by CD20 is dependent upon B cell antigen receptor signaling. *J. Biol. Chem.* **283**, 16971–16984 (2008). [doi:10.1074/jbc.M708459200](https://doi.org/10.1074/jbc.M708459200) [Medline](#)
11. D. G. Maloney, A. J. Grillo-López, C. A. White, D. Bodkin, R. J. Schilder, J. A. Neidhart, N. Janakiraman, K. A. Foon, T.-M. Liles, B. K. Dallaire, K. Wey, I. Royston, T. Davis, R. Levy, IDEC-C2B8 (rituximab) anti-CD20 monoclonal antibody therapy in patients with

- relapsed low-grade non-Hodgkin's lymphoma. *Blood* **90**, 2188–2195 (1997).
[doi:10.1182/blood.V90.6.2188](https://doi.org/10.1182/blood.V90.6.2188) [Medline](#)
12. X. Montalban, S. L. Hauser, L. Kappos, D. L. Arnold, A. Bar-Or, G. Comi, J. de Seze, G. Giovannoni, H.-P. Hartung, B. Hemmer, F. Lublin, K. W. Rammohan, K. Selmaj, A. Traboulsee, A. Sauter, D. Masterman, P. Fontoura, S. Belachew, H. Garren, N. Mairon, P. Chin, J. S. Wolinsky; ORATORIO Clinical Investigators, Ocrelizumab versus placebo in primary progressive multiple sclerosis. *N. Engl. J. Med.* **376**, 209–220 (2017).
[doi:10.1056/NEJMoa1606468](https://doi.org/10.1056/NEJMoa1606468) [Medline](#)
13. C. Klein, A. Lammens, W. Schäfer, G. Georges, M. Schwaiger, E. Mössner, K.-P. Hopfner, P. Umaña, G. Niederfellner, Epitope interactions of monoclonal antibodies targeting CD20 and their relationship to functional properties. *MAbs* **5**, 22–33 (2013).
[doi:10.4161/mabs.22771](https://doi.org/10.4161/mabs.22771) [Medline](#)
14. J. P. Deans, S. M. Robbins, M. J. Polyak, J. A. Savage, Rapid redistribution of CD20 to a low density detergent-insoluble membrane compartment. *J. Biol. Chem.* **273**, 344–348 (1998).
[doi:10.1074/jbc.273.1.344](https://doi.org/10.1074/jbc.273.1.344) [Medline](#)
15. W. G. Wierda, T. J. Kipps, J. Mayer, S. Stilgenbauer, C. D. Williams, A. Hellmann, T. Robak, R. R. Furman, P. Hillmen, M. Trneny, M. J. S. Dyer, S. Padmanabhan, M. Piotrowska, T. Kozak, G. Chan, R. Davis, N. Losic, J. Wilms, C. A. Russell, A. Österborg; Hx-CD20-406 Study Investigators, Ofatumumab as single-agent CD20 immunotherapy in fludarabine-refractory chronic lymphocytic leukemia. *J. Clin. Oncol.* **28**, 1749–1755 (2010). [doi:10.1200/JCO.2009.25.3187](https://doi.org/10.1200/JCO.2009.25.3187) [Medline](#)
16. E. Mössner, P. Brünker, S. Moser, U. Püntener, C. Schmidt, S. Herter, R. Grau, C. Gerdes, A. Nopora, E. van Puijenbroek, C. Ferrara, P. Sondermann, C. Jäger, P. Strein, G. Fertig, T. Friess, C. Schüll, S. Bauer, J. Dal Porto, C. Del Nagro, K. Dabbagh, M. J. S. Dyer, S. Poppema, C. Klein, P. Umaña, Increasing the efficacy of CD20 antibody therapy through the engineering of a new type II anti-CD20 antibody with enhanced direct and immune effector cell-mediated B-cell cytotoxicity. *Blood* **115**, 4393–4402 (2010).
[doi:10.1182/blood-2009-06-225979](https://doi.org/10.1182/blood-2009-06-225979) [Medline](#)
17. H. T. C. Chan, D. Hughes, R. R. French, A. L. Tutt, C. A. Walshe, J. L. Teeling, M. J. Glennie, M. S. Cragg, CD20-induced lymphoma cell death is independent of both caspases and its redistribution into triton X-100 insoluble membrane rafts. *Cancer Res.* **63**, 5480–5489 (2003). [Medline](#)
18. J. Du, H. Yang, Y. Guo, J. Ding, Structure of the Fab fragment of therapeutic antibody Ofatumumab provides insights into the recognition mechanism with CD20. *Mol. Immunol.* **46**, 2419–2423 (2009). [doi:10.1016/j.molimm.2009.04.009](https://doi.org/10.1016/j.molimm.2009.04.009) [Medline](#)
19. J. Du, H. Wang, C. Zhong, B. Peng, M. Zhang, B. Li, S. Hou, Y. Guo, J. Ding, Crystal structure of chimeric antibody C2H7 Fab in complex with a CD20 peptide. *Mol. Immunol.* **45**, 2861–2868 (2008). [doi:10.1016/j.molimm.2008.01.034](https://doi.org/10.1016/j.molimm.2008.01.034) [Medline](#)
20. B. Zimmerman, B. Kelly, B. J. McMillan, T. C. M. Seegar, R. O. Dror, A. C. Kruse, S. C. Blacklow, Crystal structure of a full-length human tetraspanin reveals a cholesterol-binding pocket. *Cell* **167**, 1041–1051.e11 (2016). [doi:10.1016/j.cell.2016.09.056](https://doi.org/10.1016/j.cell.2016.09.056) [Medline](#)
21. S. Nakamura, K. Irie, H. Tanaka, K. Nishikawa, H. Suzuki, Y. Saitoh, A. Tamura, S. Tsukita,

- Y. Fujiyoshi, Morphologic determinant of tight junctions revealed by claudin-3 structures. *Nat. Commun.* **10**, 816 (2019). [doi:10.1038/s41467-019-08760-7](https://doi.org/10.1038/s41467-019-08760-7) [Medline](#)
22. R. Dutzler, E. B. Campbell, M. Cadene, B. T. Chait, R. MacKinnon, X-ray structure of a ClC chloride channel at 3.0 Å reveals the molecular basis of anion selectivity. *Nature* **415**, 287–294 (2002). [doi:10.1038/415287a](https://doi.org/10.1038/415287a) [Medline](#)
23. F. Li, J. Liu, Y. Zheng, R. M. Garavito, S. Ferguson-Miller, Crystal structures of translocator protein (TSPO) and mutant mimic of a human polymorphism. *Science* **347**, 555–558 (2015). [doi:10.1126/science.1260590](https://doi.org/10.1126/science.1260590) [Medline](#)
24. T. Ramaraj, T. Angel, E. A. Dratz, A. J. Jesaitis, B. Mumey, Antigen-antibody interface properties: Composition, residue interactions, and features of 53 non-redundant structures. *Biochim. Biophys. Acta.* **1824**, 520–532 (2012).
[doi:10.1016/j.bbapap.2011.12.007](https://doi.org/10.1016/j.bbapap.2011.12.007) [Medline](#)
25. D. Ugurlar, S. C. Howes, B.-J. de Kreuk, R. I. Koning, R. N. de Jong, F. J. Beurskens, J. Schuurman, A. J. Koster, T. H. Sharp, P. W. H. I. Parren, P. Gros, Structures of C1-IgG1 provide insights into how danger pattern recognition activates complement. *Science* **359**, 794–797 (2018). [doi:10.1126/science.aoa4988](https://doi.org/10.1126/science.aoa4988) [Medline](#)
26. K. Imkeller, S. W. Scally, A. Bosch, G. P. Martí, G. Costa, G. Triller, R. Murugan, V. Renna, H. Jumaa, P. G. Kremsner, B. K. L. Sim, S. L. Hoffman, B. Mordmüller, E. A. Levashina, J.-P. Julien, H. Wardemann, Antihomotypic affinity maturation improves human B cell responses against a repetitive epitope. *Science* **360**, 1358–1362 (2018).
[doi:10.1126/science.aar5304](https://doi.org/10.1126/science.aar5304) [Medline](#)
27. D. Oyen, J. L. Torres, C. A. Cottrell, C. Richter King, I. A. Wilson, A. B. Ward, Cryo-EM structure of *P. falciparum* circumsporozoite protein with a vaccine-elicited antibody is stabilized by somatically mutated inter-Fab contacts. *Sci. Adv.* **4**, eaau8529 (2018).
[doi:10.1126/sciadv.aau8529](https://doi.org/10.1126/sciadv.aau8529) [Medline](#)
28. T. Tamada, D. Shinmi, M. Ikeda, Y. Yonezawa, S. Kataoka, R. Kuroki, E. Mori, K. Motoki, TRAIL-R2 superoligomerization induced by human monoclonal agonistic antibody KMTR2. *Sci. Rep.* **5**, 17936 (2015). [doi:10.1038/srep17936](https://doi.org/10.1038/srep17936) [Medline](#)
29. L. C. Simmons, D. Reilly, L. Klimowski, T. S. Raju, G. Meng, P. Sims, K. Hong, R. L. Shields, L. A. Damico, P. Rancatore, D. G. Yansura, Expression of full-length immunoglobulins in *Escherichia coli*: Rapid and efficient production of aglycosylated antibodies. *J. Immunol. Methods* **263**, 133–147 (2002). [doi:10.1016/S0022-1759\(02\)00036-4](https://doi.org/10.1016/S0022-1759(02)00036-4) [Medline](#)
30. G. B. Fields, R. L. Noble, Solid phase peptide synthesis utilizing 9-fluorenylmethoxycarbonyl amino acids. *Int. J. Pept. Protein Res.* **35**, 161–214 (1990).
[doi:10.1111/j.1399-3011.1990.tb00939.x](https://doi.org/10.1111/j.1399-3011.1990.tb00939.x) [Medline](#)
31. T. Grant, A. Rohou, N. Grigorieff, *cisTEM*, user-friendly software for single-particle image processing. *eLife* **7**, e35383 (2018). [doi:10.7554/eLife.35383](https://doi.org/10.7554/eLife.35383) [Medline](#)
32. D. N. Mastronarde, Automated electron microscope tomography using robust prediction of specimen movements. *J. Struct. Biol.* **152**, 36–51 (2005). [doi:10.1016/j.jsb.2005.07.007](https://doi.org/10.1016/j.jsb.2005.07.007) [Medline](#)

33. P. Emsley, B. Lohkamp, W. G. Scott, K. Cowtan, Features and development of *Coot*. *Acta Crystallogr. Sect. D Biol. Crystallogr.* **66**, 486–501 (2010). [doi:10.1107/S0907444910007493](https://doi.org/10.1107/S0907444910007493) [Medline](#)
34. T. I. Croll, *ISOLDE*: A physically realistic environment for model building into low-resolution electron-density maps. *Acta Crystallogr. Sect. D Struct. Biol.* **74**, 519–530 (2018). [doi:10.1107/S2059798318002425](https://doi.org/10.1107/S2059798318002425) [Medline](#)
35. P. V. Afonine, B. K. Poon, R. J. Read, O. V. Sobolev, T. C. Terwilliger, A. Urzhumtsev, P. D. Adams, Real-space refinement in *PHENIX* for cryo-EM and crystallography. *Acta Crystallogr. Sect. D Struct. Biol.* **74**, 531–544 (2018). [doi:10.1107/S2059798318006551](https://doi.org/10.1107/S2059798318006551) [Medline](#)
36. R. Norel, S. L. Lin, H. J. Wolfson, R. Nussinov, Shape complementarity at protein-protein interfaces. *Biopolymers* **34**, 933–940 (1994). [doi:10.1002/bip.360340711](https://doi.org/10.1002/bip.360340711) [Medline](#)
37. T. D. Goddard, C. C. Huang, E. C. Meng, E. F. Pettersen, G. S. Couch, J. H. Morris, T. E. Ferrin, UCSF ChimeraX: Meeting modern challenges in visualization and analysis. *Protein Sci.* **27**, 14–25 (2018). [doi:10.1002/pro.3235](https://doi.org/10.1002/pro.3235) [Medline](#)
38. L. Holm, Benchmarking fold detection by DaliLite v.5. *Bioinformatics* **35**, 5326–5327 (2019). [doi:10.1093/bioinformatics/btz536](https://doi.org/10.1093/bioinformatics/btz536) [Medline](#)
39. F. Madeira, Y. M. Park, J. Lee, N. Buso, T. Gur, N. Madhusoodanan, P. Basutkar, A. R. N. Tivey, S. C. Potter, R. D. Finn, R. Lopez, The EMBL-EBI search and sequence analysis tools APIs in 2019. *Nucleic Acids Res.* **47**, W636–W641 (2019). [doi:10.1093/nar/gkz268](https://doi.org/10.1093/nar/gkz268) [Medline](#)
40. G. Cardone, J. B. Heymann, A. C. Steven, One number does not fit all: Mapping local variations in resolution in cryo-EM reconstructions. *J. Struct. Biol.* **184**, 226–236 (2013). [doi:10.1016/j.jsb.2013.08.002](https://doi.org/10.1016/j.jsb.2013.08.002) [Medline](#)